Supporting Information

Rational Catalyst Layers Design Enables Tailored Transport Channels for Efficient CO_2 Electrochemical Reduction to Multi-carbon Products

Jiping Sun [a, b], Bichao Wu [a], Zhixing Wang [a, c], Huajun Guo [a, c], Guochun Yan [a, c], Hui Duan [a, c], Guangchao Li [a, c], Ying Wang [b, *] and Jiexi Wang [a, c, *]

[a] *National Energy Metal Resources and New Materials Key Laboratory, Engineering Research Center of the Ministry of Education for Advanced Battery Materials, Hunan Provincial Key Laboratory of Nonferrous Value-Added Metallurgy, School of Metallurgy and Environment, Central South University, Changsha 410083, P. R. China.*

[b] *Department of Chemistry, The Chinese University of Hong Kong, Hong Kong 999077, S. A. R., China.*

[c] *National Engineering Research Centre of Advanced Energy Storage Materials, Changsha, 410205, P. R. China.*

* Corresponding author, email address: Ying Wang, ying.b.wang@cuhk.edu.hk; Jiexi Wang, wangjiexikeen@csu.edu.cn.

Experimental Section

Chemicals and materials

Copper nanoparticle (Cu NPs, Sigma, 25 nm), SSC-D72 ionomer (Aquivion, D72-25BS), SSC-D79 ionomer (Aquivion, D72-25BS), LSC-D520 ionomer (DuPont, D-520, 5 wt%), LSC-D521 ionomer (Dupont, D-521, 5 wt%), Isopropanol (IPA, Hushi, AR, ≥ 99.7%), Deionized water (DIW, 18.25 MΩ cm), Potassium bicarbonate (Aladdin, AR, 99.5%), Dimethyl sulfoxide (DMSO, Sigma, anhydrous, ≥ 99.9%), Deuterated water (D_2O, Aladdin, 99.9 atom % D), Carbon paper (GDL, Sinero, YLS-30T), Anion-exchange membrane (AEM, Dioxide Materials, Sustainion X37-50 Grade RT, 50 μm), and Anion-exchange membrane (AEM, Alkymer, W-25, 25 μm). All the chemical reagents and materials were purchased from commercial suppliers and used as received.

Preparation of Cu-GDE

Taking D520-20/1 as an example, 20 mg Cu NPs, 215 μL LSC-D520 ionomer solution (10 times diluted, the ionomer/catalyst mass ratio is 1/20) and 1785 μL solvent (Isopropanol: H_2O= 2:1, volume ratio) were mixed and sonicated for 1 hour in cold water to prepare the uniform catalyst ink. To prevent errors caused by the viscosity of the ionomer solution, all ionomer solutions were used after dilution. The inks with different SSC and LSC ionomers were marked as SSC-D72, SSC-D79, LSC-D520, and LSC-D521 according to the ionomer type. The ionomer content was regulated to obtain ink with different C/I ratios. The inks of LSC-D520 with different C/I ratios were prepared and named D520-5/1, 10/1, 20/1, and 40/1. The GDEs were prepared by spraying catalyst ink onto carbon paper GDLs at the speed of 2000 mm min^{-1}. High-purity nitrogen (N_2) was used as a spray carrier gas to prevent GDE pollution. The cathode GDEs were obtained after vacuum drying overnight at 40 °C. The effective geometric area of Cu-GDEs was 4 cm^2 (2cm×2cm) and the actual catalyst loading was controlled at around 0.5 mg cm^{-2}. For the amplification experiments, the

effective geometric area of the cathode GDE was 81 cm^2 (9cm×9cm) with a loading of 0.5 mg cm^{-2}.

Materials characterization

A double Spherical Aberration Corrected Transmission Electron Microscope (AC-TEM, Titan G2 60-300) coupled with an energy dispersive spectrometer (EDS) and HAADF-STEM was employed to characterize the morphology of the catalyst ink. Dynamic Light Scattering (DLS, Malvern Zetasizer Nano ZS90) was used to detect the colloidal particle size of the ink. Thus, the hydrodynamic diameter (D_h) and particle size distribution of the ink were obtained. 5 μL ink was diluted with 5 mL solvent (Isopropanol: H_2O= 2:1, volume ratio) to avoid light scattering. A modular Compact Rheometer (MCR, Anton Paar MCR 302e) was adopted to carry out the rheological measurements of the catalyst ink. Atomic Force Microscope (AFM, Bruker Dimension Edge™) was employed to obtain the surface geometry imaging of CLs. Cu foil was chosen as the substrate, and the catalyst ink was dripped onto the smooth blank Cu foil. Scanning Electron Microscope (SEM, JEOL JSM-7900F) coupled with EDS was used to characterize the morphology of the Cu-GDE. The contact angle test was carried out to evaluate the hydrophilicity of the CL surface. Wide Angle X-ray scattering apparatus (WAXS, Xenocs Xeuss 2.0) with detector (Pilatus 3R 300K) and Raman spectrum (Raman, Thermo Scientific DXR) were used to characterize the electronic structure of GDEs. The surface chemical structure of the GDEs was determined by X-ray Photoelectron Spectroscopy (XPS, Thermo Scientific ESCALAB Xi+) with Al Kα radiation. All the spectra were calibrated against C 1s (284.8 eV). The pore size distribution of GDEs was detected by the high-performance automatic mercury injection instrument (MIP, Micromeritics AutoPore IV 9510). All the tests were carried out at room temperature (25 °C).

Calculation method

The density functional theory (DFT) calculation method was used to evaluate the adsorption energy of LSC and SSC ionomers with CO_2 and H_2O. The CASTEP first-principles implementation was employed for the calculations. The exchange-correlation potential was calculated using the generalized gradient approximation (GGA) with the Perdew–Burke–Ernzerhof (PBE) formula, in conjunction with the DFT-D correction. The Broyden–Fletcher–Goldfarb–Shanno (BFGS) method was employed to identify the ground state of the supercells, and the convergence tolerance was set to an energy change of less than 10^{-5} eV. The cutoff energy of the atomic wave functions was set to 450 eV. Subsequently, all molecular structures were calculated following the completion of the geometry optimization process.

Molecular dynamics simulation

Molecular dynamics (MD) simulation was employed to model the appetency of different ionomers with CO_2 and H_2O in the catalyst layer. The simulation condition was 298.15 K at 1 atm using the COMPASS III force field with force type and charges. A further 5 ns was run to collect data for statistical analysis in the NVT ensemble once the system was fully equilibrated. The degree of the polymerization of the ionomers is 10, and the solvent system employed in the actual experiments corresponds to this value (isopropanol/water = 2:1, volume ratio).

In-situ Surface-enhanced infrared spectroscopy (In-situ ATR-SEIRAS)

The ATR-SEIRAS technique was employed using a Nicolet iS50 FTIR spectrometer, equipped with a narrow-band MCT-A detector and an in-situ IR optical accessory (SPEC-II, Shanghai Yuanfang Tech.), at an incidence angle of approximately 60°. CO_2 gas was introduced at room temperature, and the background spectrum was collected 20 min after the introduction of CO_2. The electrolyte was a CO_2-saturated 0.1M $KHCO_3$ solution, with a platinum mesh and a saturated calomel electrode used as the counter electrode (CE) and the

reference electrode (RE), respectively. The IR spectra were collected with unpolarised IR radiation at a spectral resolution of 16 cm^{-1}. All spectra were presented in absorbance, defined as the negative natural logarithm of the ratio of the sample and reference single-beam spectra, respectively. A CHI 440 electrochemistry workstation (CH Instruments, Inc.) was employed for potential control and current measurements.

Electrochemical measurements

The electrochemical measurements were conducted in an MEA-based electrolyzer. MEA was assembled by two electrode plates, Cu-GDE cathode, anion-exchange membrane (AEM), IrO_2/Ti anode, and tetrafluoride gaskets. The flow field plates of the cathode and anode were titanium metal plates. A cation exchange ionomer (CEI) PFSA was employed as an ionomer binder to transfer protons and bond catalysts. The effective geometric area of the Cu-GDE cathode was 4 cm^2 (2cm×2cm). For the amplification experiments, the effective geometric area of the cathode GDE was 81 cm^2 (9cm×9cm). The Au-coated Cu plate was used in the cathode for current collecting. The IrO_2-coated Ti foam was used as the anode for the oxygen evolution reaction (OER), and IrO_2 loading was 2 mg cm^{-2}. A 50μm Sustainion AEM and a 25 μm Alkymer AEM were employed to separate the cathode and anode in conditional inquiry tests and optimization tests respectively. 0.1 M $KHCO_3$ solution was adopted as anolyte with a flow rate of 15 mL min^{-1}. High-purity carbon dioxide (99.99%, Linde) was continuously supplied to the backside of Cu-GDE at a flow rate of 45 sccm. The CO_2 gas was humidified in a 50 °C water bath and bubbled for a long time before the reaction started. The electrolysis was carried out at 50 °C. All the electrochemical measurements were conducted on a ZAHNER ZENNIUM pro potentiostat. The CO_2RR activity was tested by linear scanning voltammetry (LSV) methods. The CO_2RR selectivity and stability of Cu-GDEs were tested by chronoamperometry and chronopotentiometry methods. Cyclic voltammetry (CV) test at different scan rates of different ionomers was carried

out with the scan rate of 5, 10, 20, 40, 60, 80, 100, 120, 140 mV s^{-1}. Electrochemical impedance spectroscopy (EIS) was employed at a constant potential and the frequency of 10 to 10000 Hz. As for the amplification experiments (81 cm^2), the electrochemical measurements were conducted on a DC power supply (ABF KPS3020D 30V20A).

Product analysis

Gas products were analyzed by an online gas chromatography (GC, Ramiin GC 2060) equipped with a TCD detector for H_2 and an FID detector for CO, CH_4, and C_2H_4. Online differential electrochemical mass spectroscopy (DEMS, Pfeiffer PrismaPro QMG 250) was used to characterize the hydrogen evolution reaction (HER), CO_2RR, and limiting current density of ethylene during LSV scanning. The calibration lines of GC and *in-situ* DEMS were both made by the external standard method. Liquid products were collected with flow-out electrolyte and analyzed by an offline 1H nuclear magnetic resonance (NMR) spectrometer (Brucker AVANCE III HD 500), with dimethyl sulfoxide (DMSO) as an internal standard. The Faraday efficiencies (FE_S) of the products were calculated using the following formula:

$$FE_i = \frac{Q_i}{Q_{total}} = \frac{Z_i \times n_i \times F}{Q_{total}} \times 100\% \quad (1)$$

Where,

Q_i: the charge used for a specific product i;

Q_{total}: the total amount of charge passed during the electrolysis;

Z_i: the molar amount of the product i;

F: the Faradaic constant (96,485 C mol^{-1});

n_i: the number of electron transfers when the product i is formed.

The partial current densities (J_i) of the products were calculated using the following formula:

$$J_i = \frac{FE_i \times I}{S} = FE_i \times j \quad (2)$$

Where,

FE_i: the Faraday Efficiencies of the products;

I: the applied current of the system;

S: effective geometric area of the Cu-GDE cathode;

j: the applied current densities of the cathode.

The energy efficiencies (EES) of C_{2+} products were calculated using the following formula:

$$EE_{C2+} = \sum i \frac{E_{0(i)} \times FE_i}{V_{cell}} \times 100\% \quad (3)$$

Where,

V_{cell}: the applied cell potential of the MEA electrolyzer;

$E_{0(i)}$: the equilibrium potential for different CO_2RR-to-C_{2+} reactions;

FE_i: the Faraday Efficiencies of various C_{2+} products.

The water flux (X_{H_2O}) of the membrane in MEA at different current densities was quantified using the following formula[1]:

$$X_{H_2O,\,cathode} = X_{H_2O,\ total\ outlet} - X_{H_2O,\ \ CO_2\ feed} \quad (4)$$

Where,

$X_{H_2O,\ total\ outlet}$: the total water flux of the outlet which is used for the reaction;

$X_{H_2O,\ \ CO_2\ feed}$: the water flux contributed by the humidified CO_2 feed.

Figures

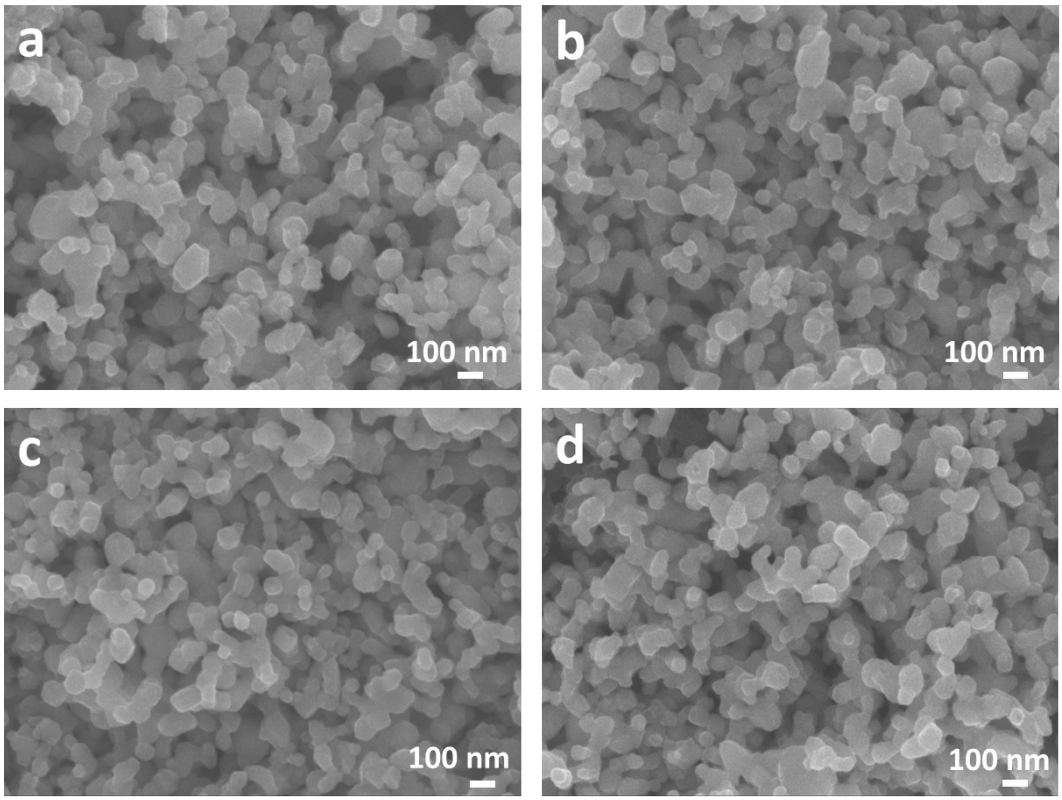

Fig. S1. SEM images of catalyst layers with different types of ionomers at C/I ratio of 10/1. (a) SSC-D72, (b) SSC-D79, (c) LSC-D520, and (d) LSC-D521.

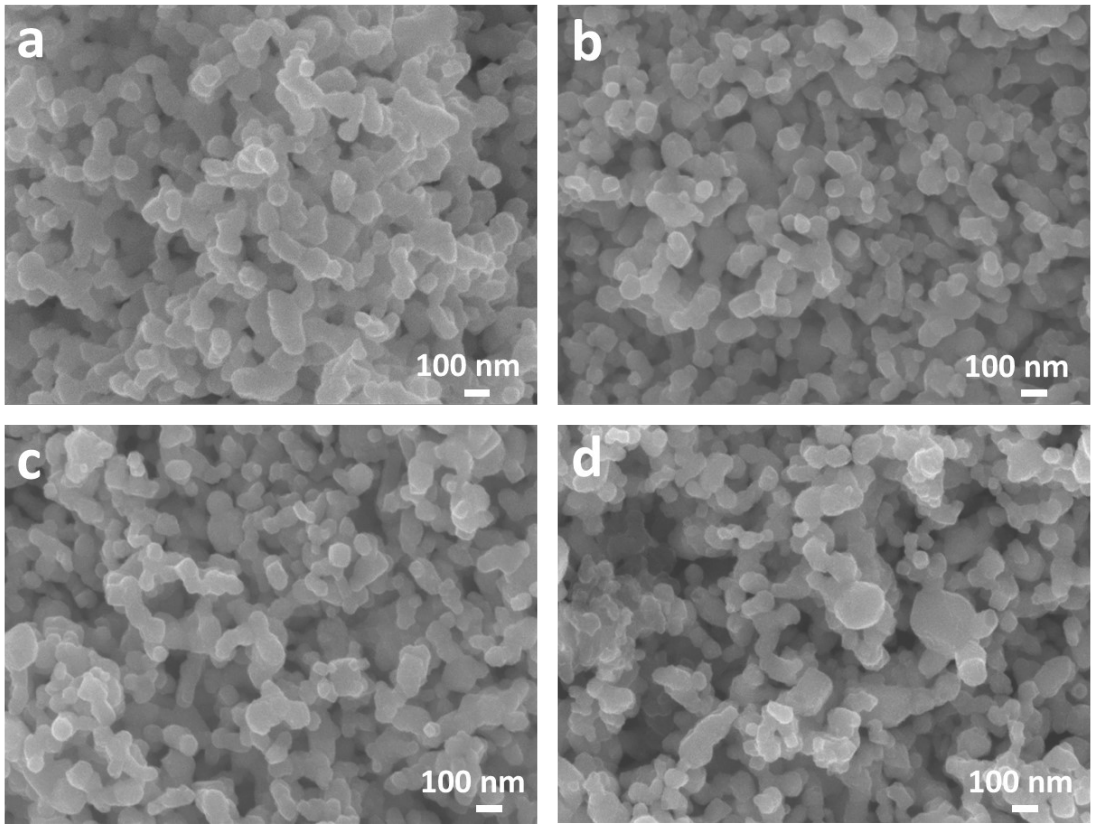

Fig. S2. SEM images of catalyst layers with different C/I ratios of LSC-D520. (a) C/I ratio= 5/1, (b) C/I ratio= 10/1, (c) C/I ratio= 20/1, and (d) C/I ratio= 40/1.

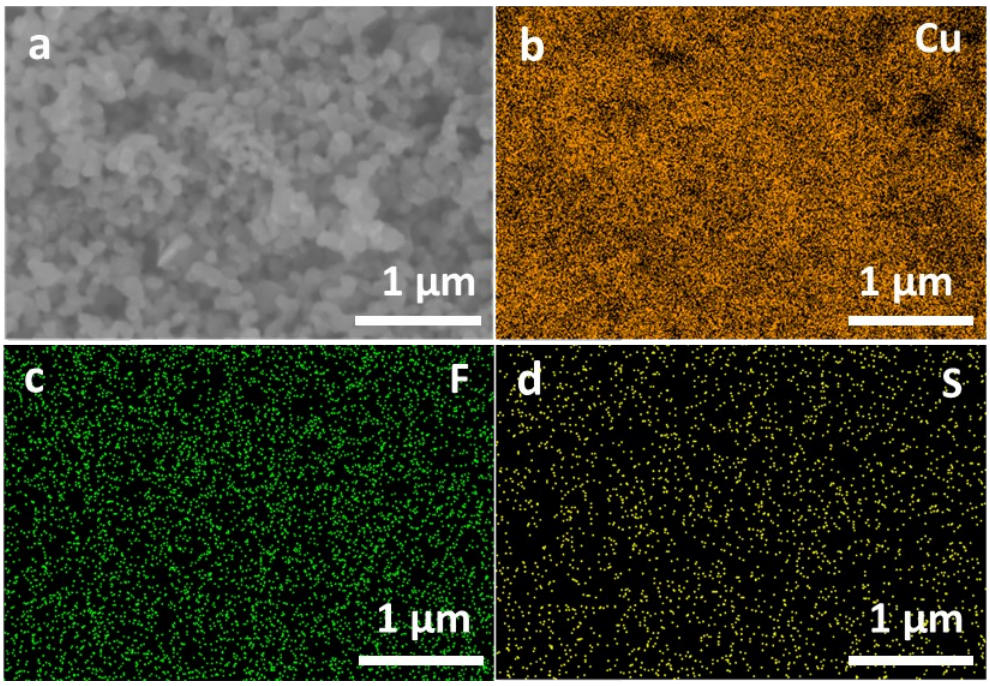

Fig. S3. SEM images and EDS mapping of the LSC-D520-20/1 gas diffusion electrode (GDE) surface. (a) Surface morphology; Surface elements distribution of (b) Cu, (c) F, and (d) S.

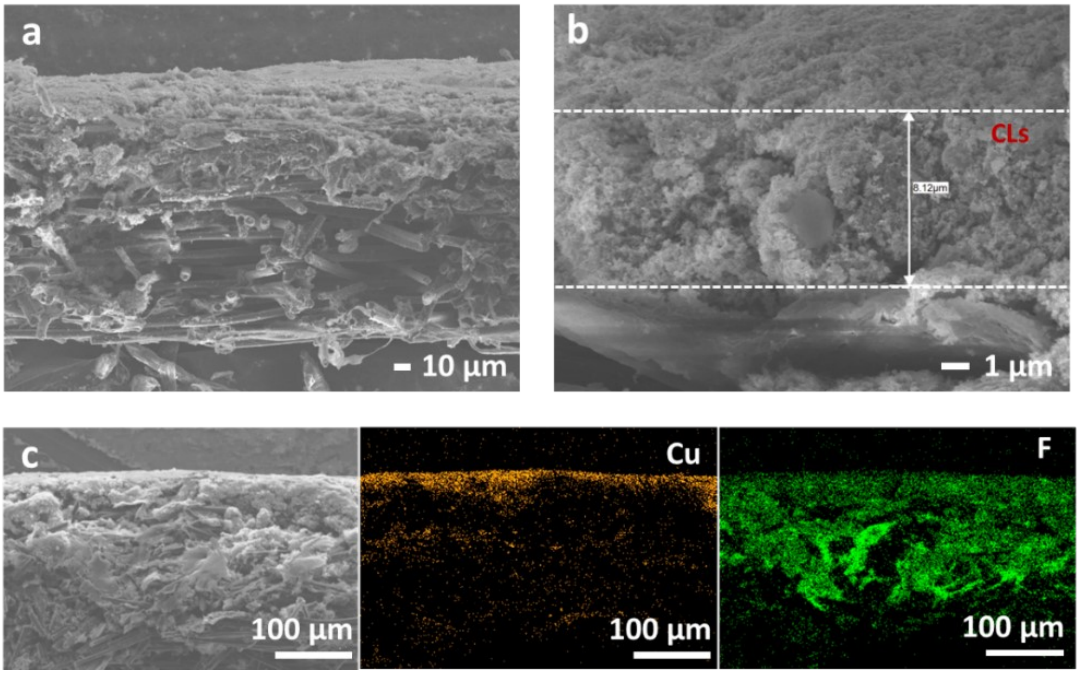

Fig. S4. SEM micrograph and EDS mapping of cross-section morphology of LSC-D520-20/1 GDE. (a-b) Cross-section microstructure; (c) Elements distribution of Cu and F.

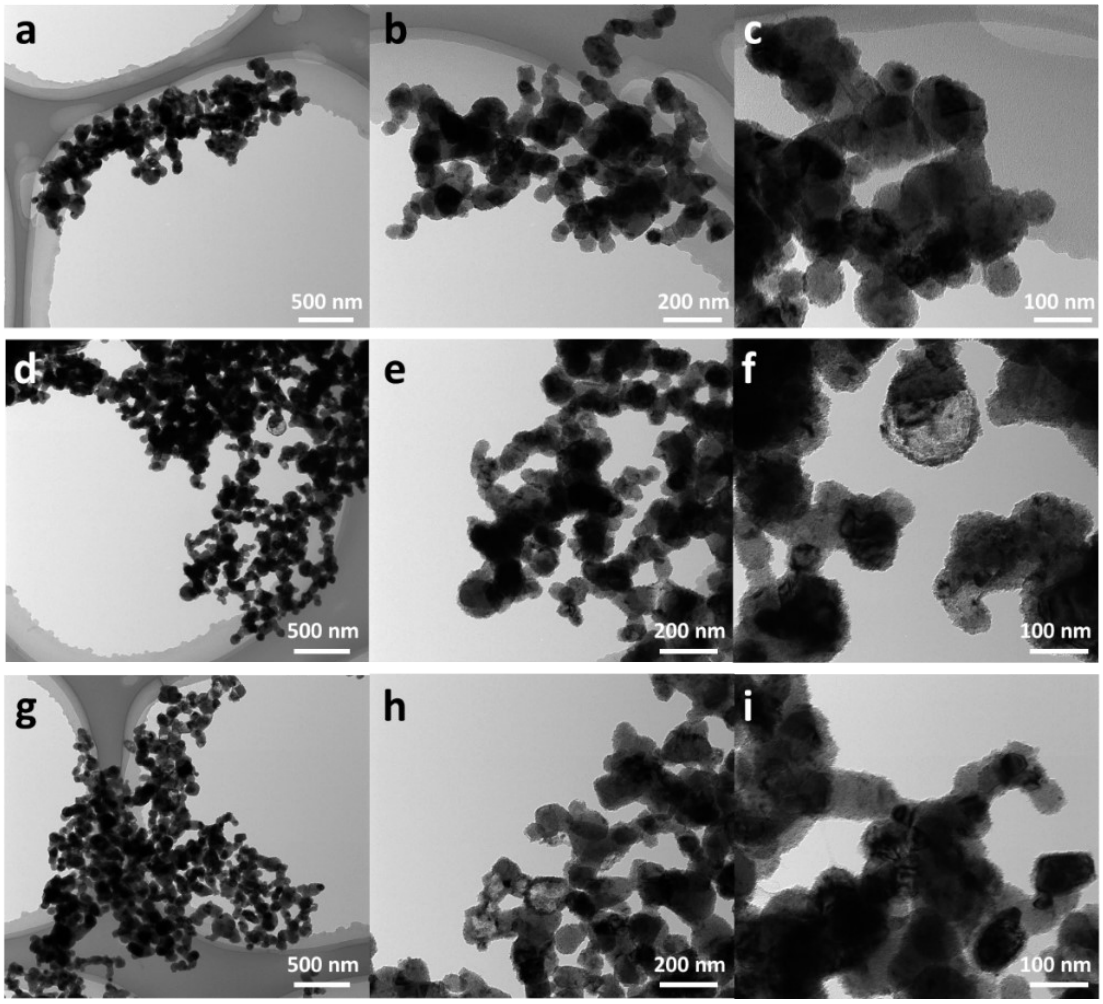

Fig. S5. AC-TEM micrograph of (a-c) SSC-D72, (d-f) SSC-D79, and (g-i) LSC-D521. (C/I ratio=10/1)

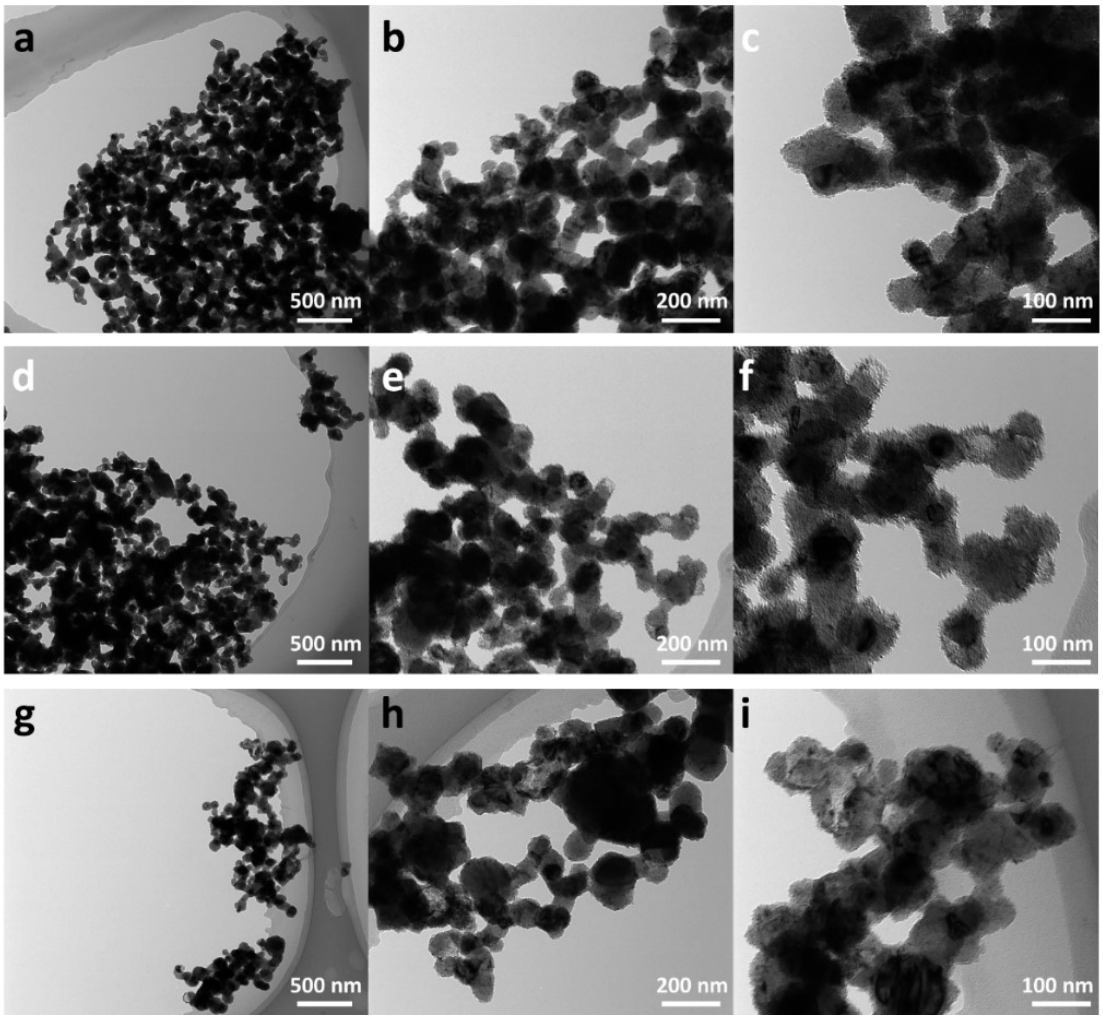

Fig. S6. AC-TEM micrograph of (a-c) LSC-D520-10/1, (d-f) LSC-D520-40/1, and (g-i) LSC-D520-5/1.

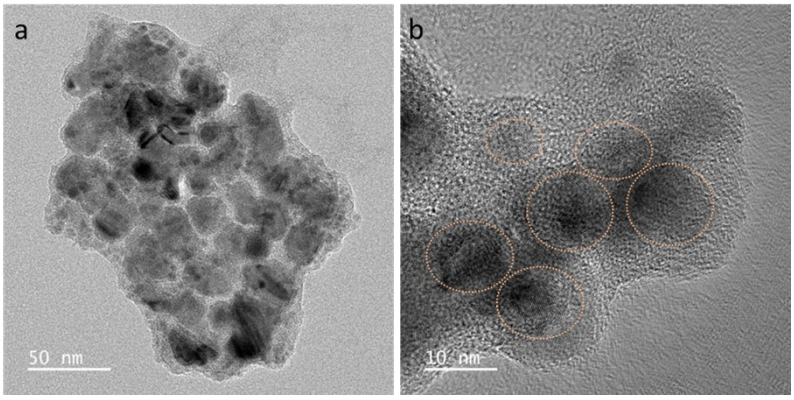

Fig. S7. TEM (a) and HR-TEM (b) images of LSC-D520-20/1 samples.

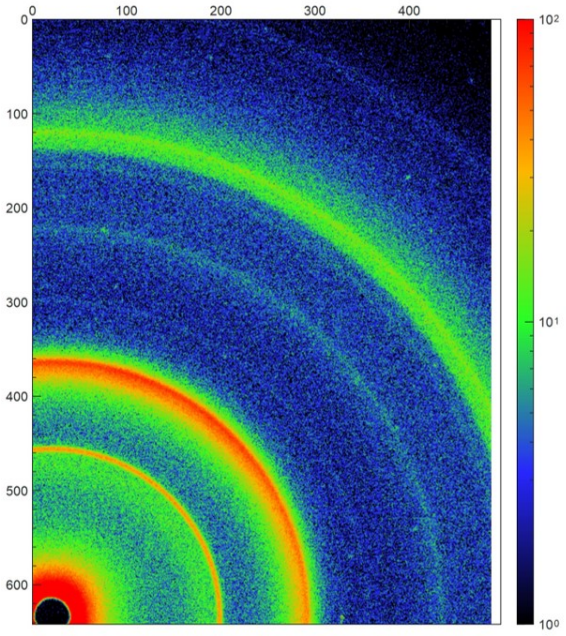

Fig. S8. 2D WAXS patterns of D520-20/1 GDE.

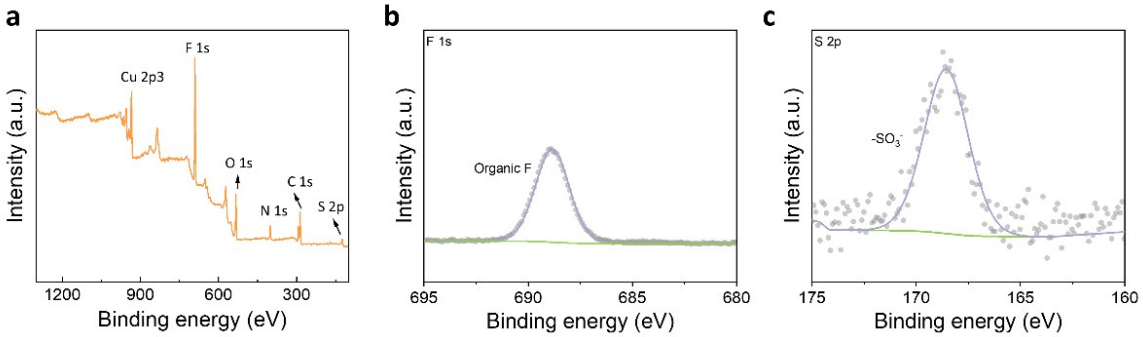

Fig. S9. (a) XPS full survey, (b) F 1s spectra, and (c) S 2p spectra of D520-20/1 GDE.

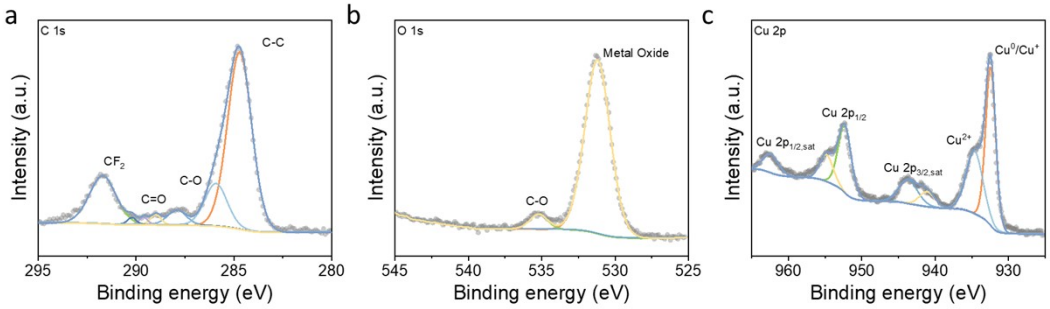

Fig. S10. XPS results of Cu-GDE without PFSA ionomer. (a) C 1s, (b) O 1s, and (c) Cu 2p spectra.

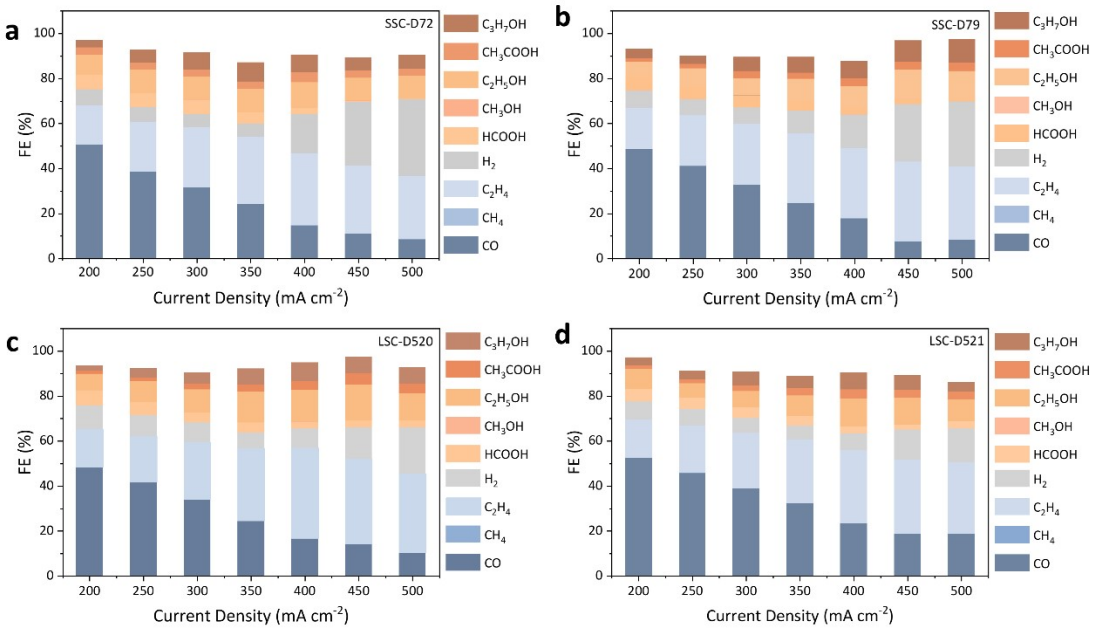

Fig. S11. Product distribution of different ionomers at different current densities. (a) SSC-D72, (b) SSC-D79, (c) LSC-D520, (d) LSC-D521.

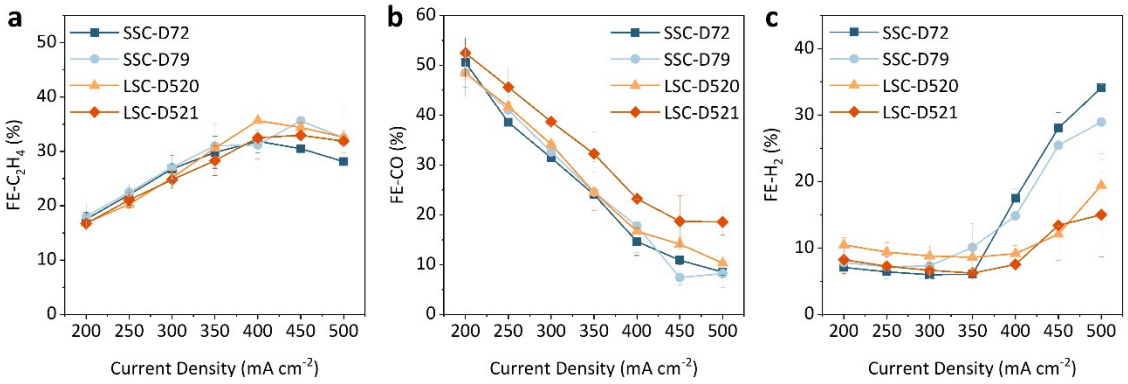

Fig. S12. FE-C_2H_4/CO/H_2 of different ionomers. (a) FE-C_2H_4, (b) FE-CO, (c) FE-H_2.

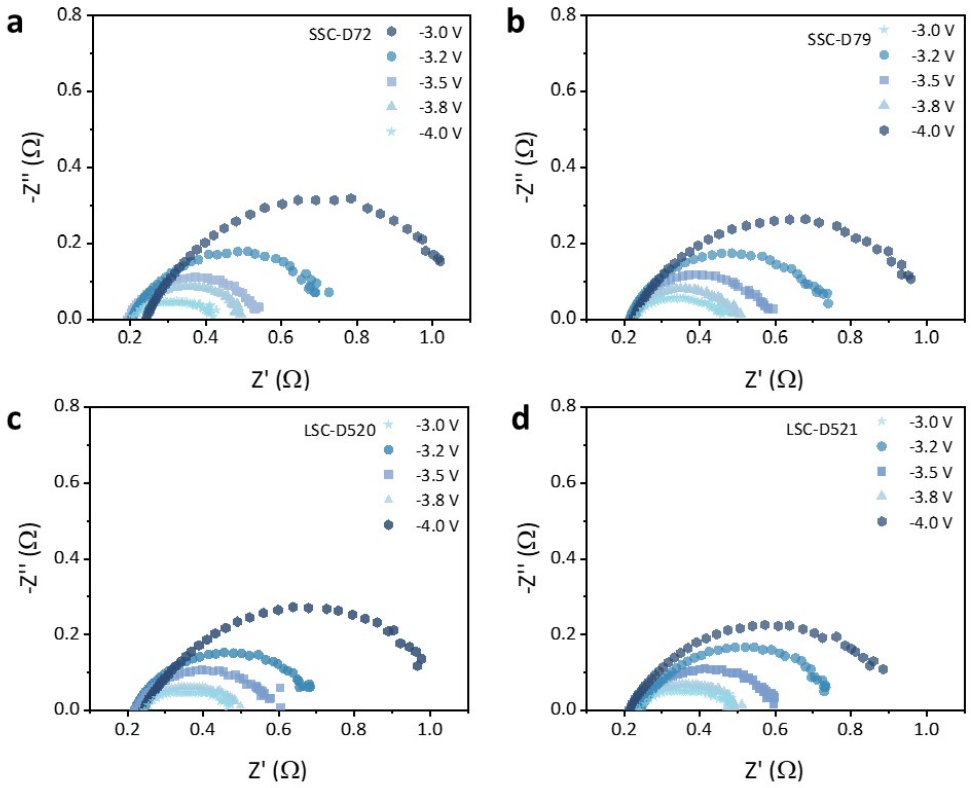

Fig. S13. EIS results of different ionomers at different cell voltages. (a) SSC-D72, (b) SSC-D79, (c) LSC-D520, (d) LSC-D521.

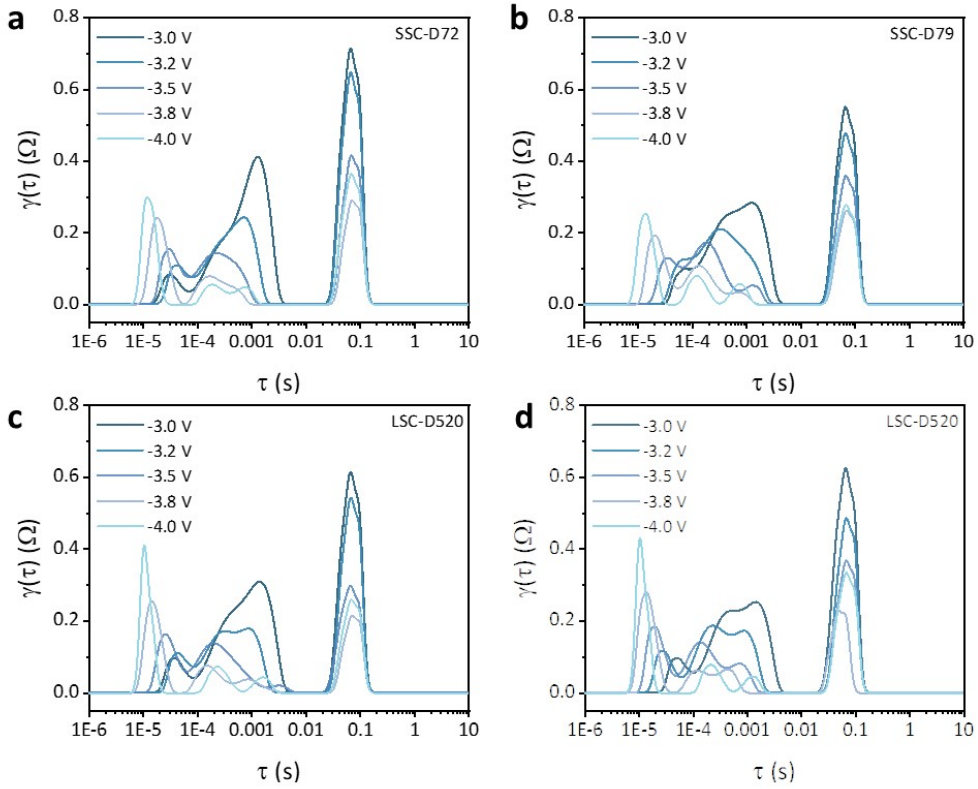

Fig. S14. DRT results of different ionomers at various cell voltages. (a) SSC-D72, (b) SSC-D79, (c) LSC-D520, (d) LSC-D521.

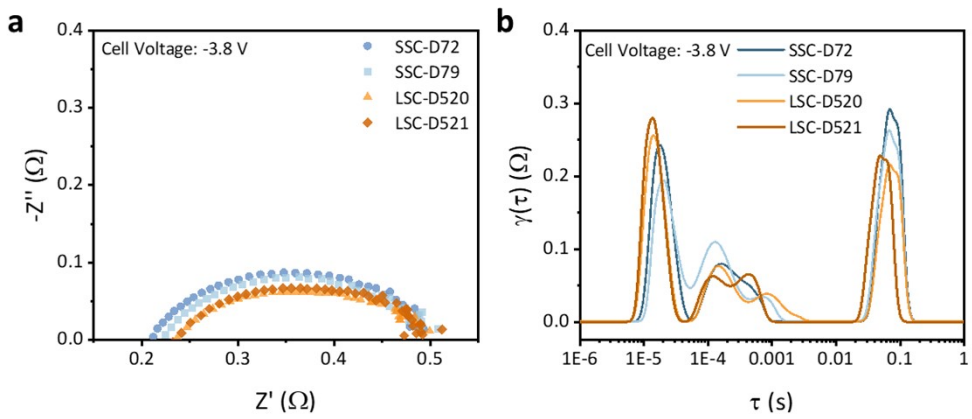

Fig. S15. EIS and DRT results of different ionomers at -3.8 V.

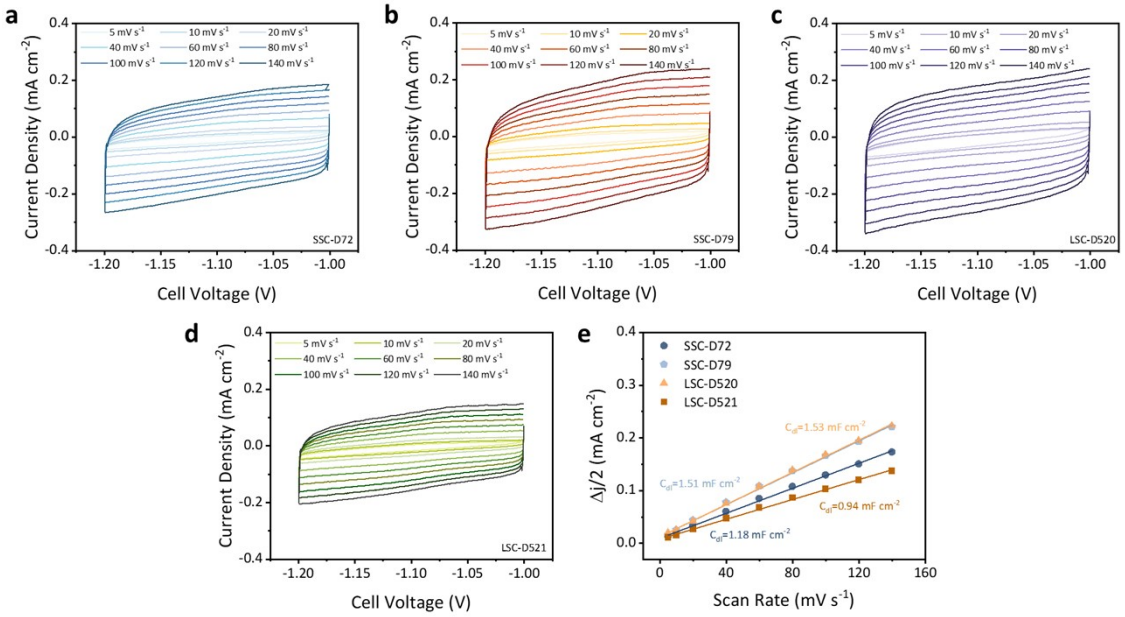

Fig. S16. (a-d) CV curves at different scan rates of SSC-D72, SSC-D79, LSC-D520, and LSC-D521. (e) The double-layer capacitance of different ionomers.

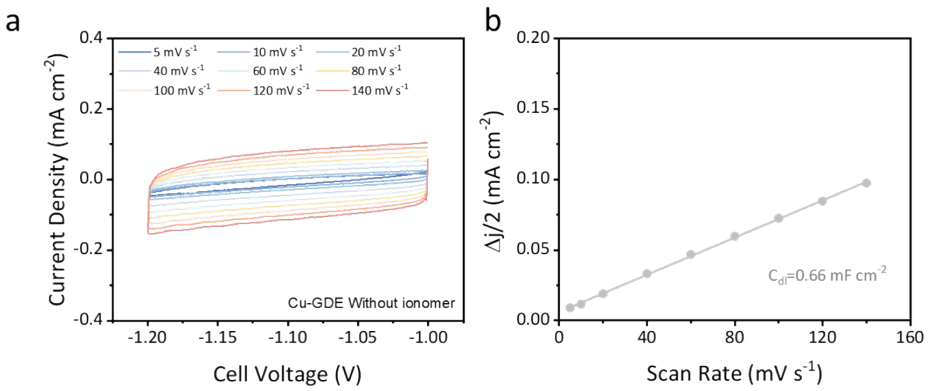

Fig. S17. (a) CV curves at different scan rates of Cu-GDE without ionomer. (b) The double-layer capacitance of Cu-GDE without ionomer.

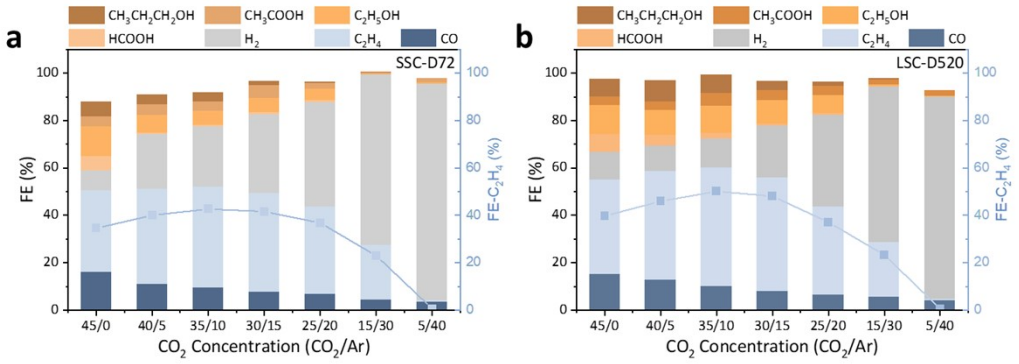

Fig. S18. Product distribution of (a) SSC-D72 and (b) LSC-D520 at different CO_2 concentrations.

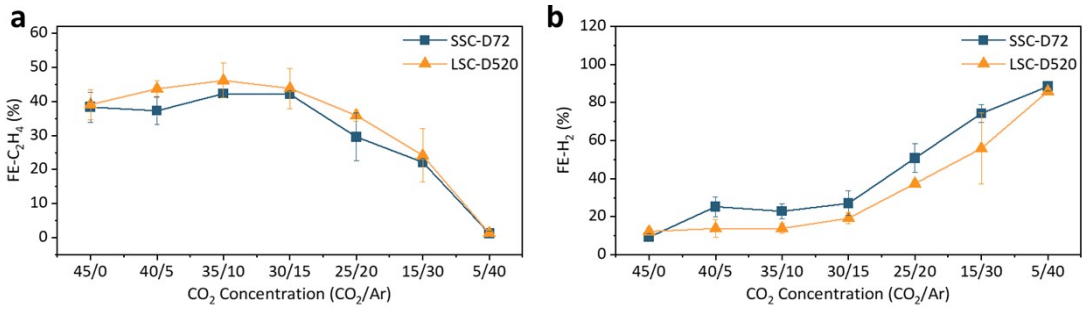

Fig. S19. Performance comparison of SSC-D72 and LSC-D520 at different CO_2 concentrations. (a) FE-C_2H_4, (b) FE-H_2.

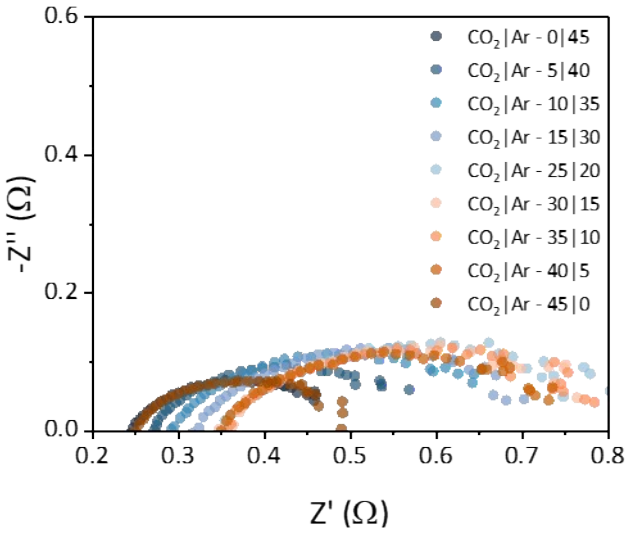

Fig. S20. EIS results of LSC-D520 at different CO_2 concentration.

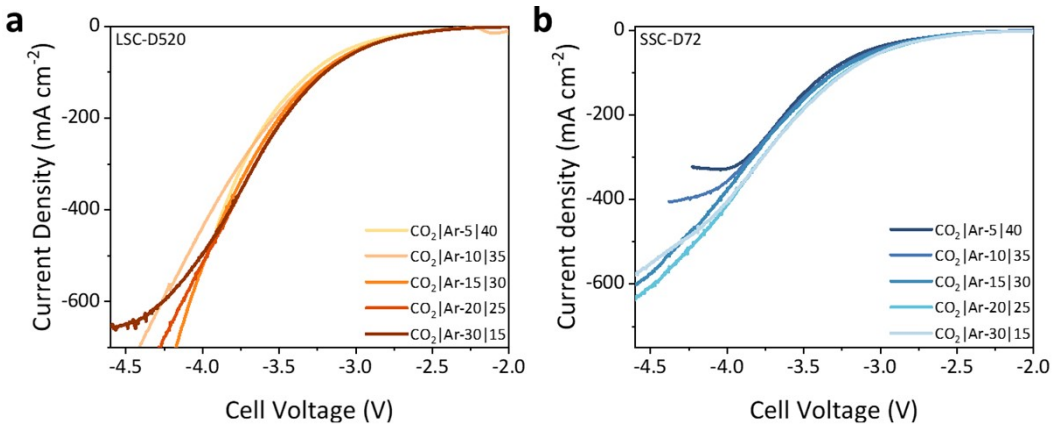

Fig. S21. LSV curves of (a) LSC-D520 and (b) SSC-D72 at various low CO_2 concentrations.

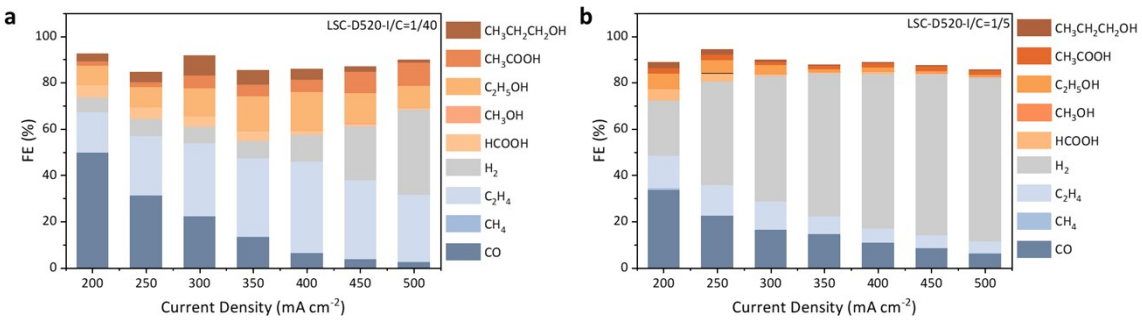

Fig. S22. Product distribution of different C/I ratios at different current densities. (a) C/I=40/1, (b) C/I=5/1.

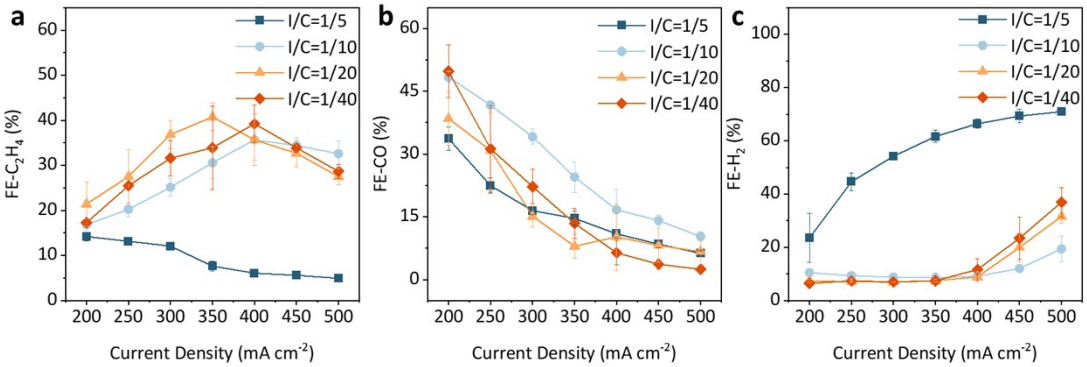

Fig. S23. FE-C_2H_4/CO/H_2 of different C/I ratio of LSC-D520. (a) FE-C_2H_4, (b) FE-CO, (c) FE-H_2.

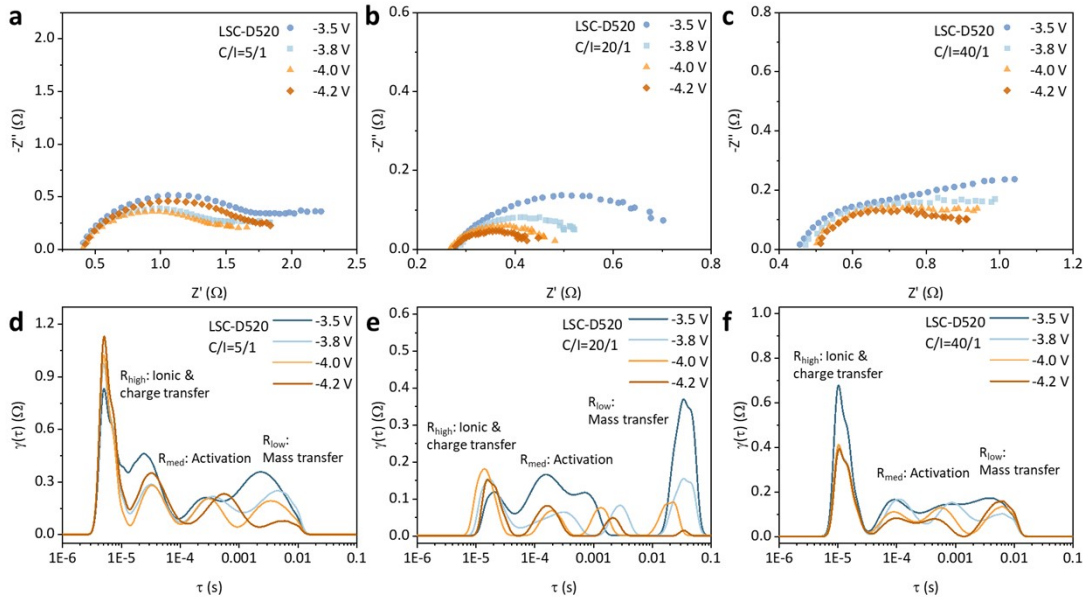

Fig. S24. EIS and DRT results of different C/I ratios of LSC-D520. (a, d) C/I=5/1, (b, e) C/I=20/1, (c, f) C/I=40/1.

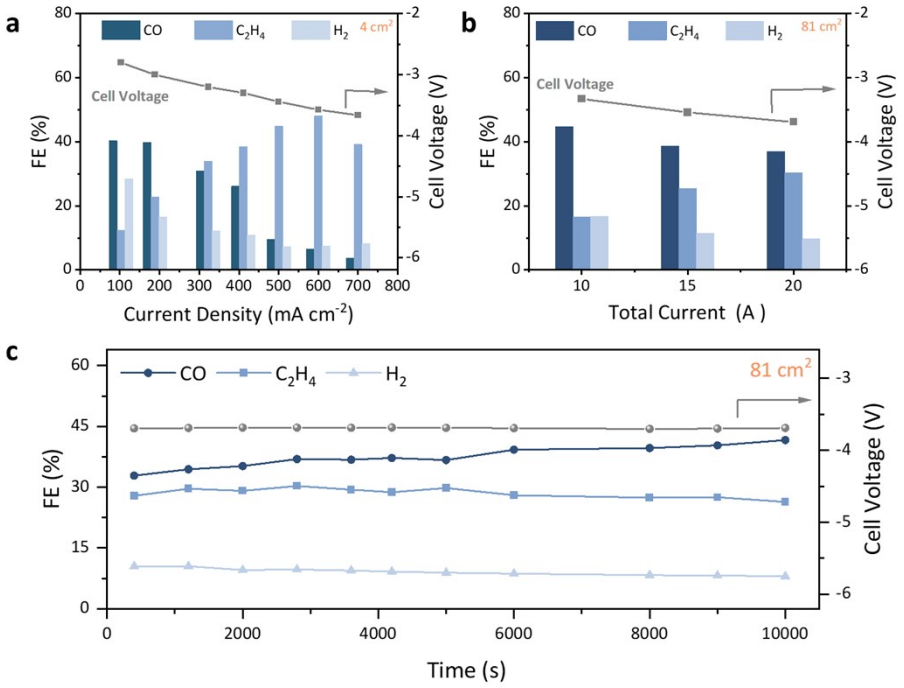

Fig. S25. Scale-up of LSC-D520-C/I=20/1. (a) 4 cm^2, (b) 81 cm^2, (c) Stability of 81 cm^2.

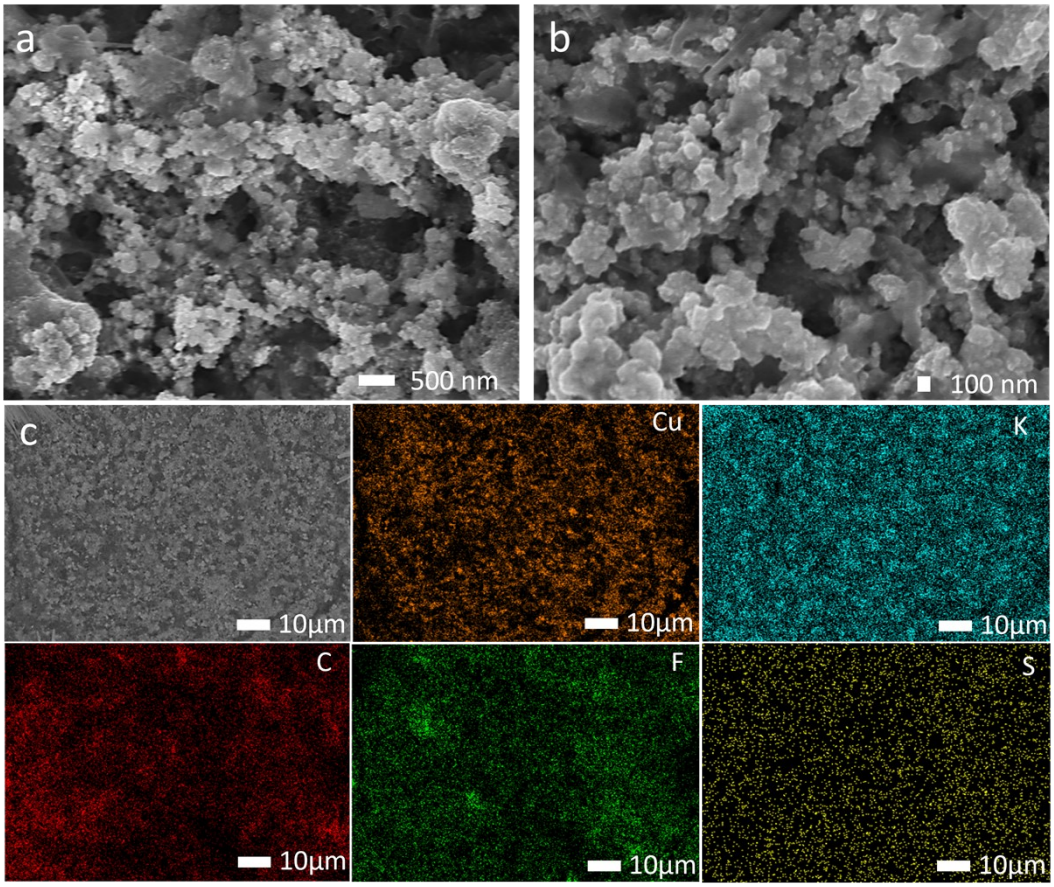

Fig. S26. The SEM images (a, b) and EDS mapping (c) of LSC-D520 Cu-GDEs surface after long-time electrolysis.

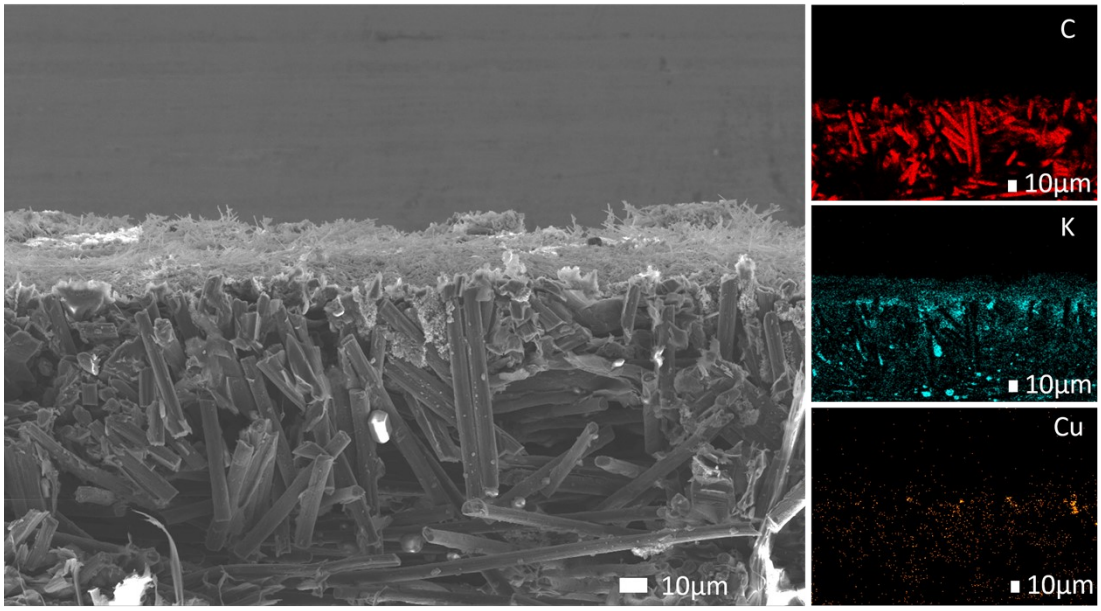

Fig. S27. SEM micrograph and EDS mapping of cross-section morphology of LSC-D520 Cu-GDEs after long-time electrolysis.

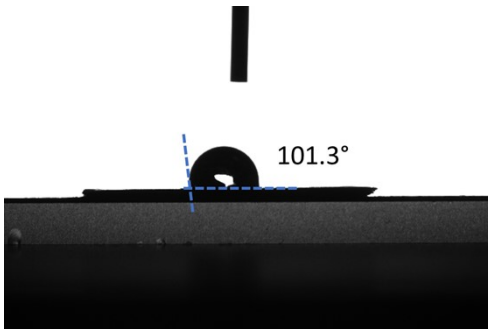

Fig. S28. XPS results of the LSC-D520 Cu-GDEs surface after long-time electrolysis.

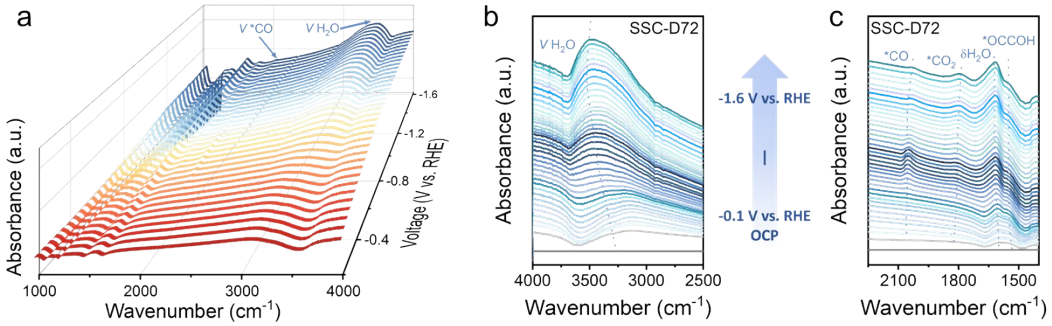

Fig. S29. *In-situ* ATR-SEIRAS of SSC-D72 (a), and magnified image of (b) signal of H_2O and (c) signal of CO_2.

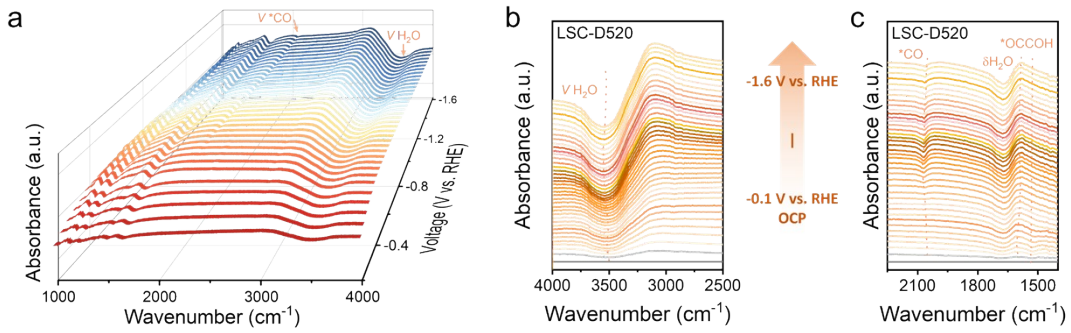

Fig. S30. *In-situ* ATR-SEIRAS of LSC-D520 (a), and magnified image of (b) signal of H_2O and (c) signal of CO_2.

Tables

Table S1. Elements content analysis of LSC-D520-20/1 GDE surface based on EDS results corresponding to Fig. S3.

Sample	C	F	S	Cu
	Wt%			
LSC-D520-20/1	9.12	2.90	0.10	87.88

Table S2. Volume distribution of the particle size in the catalyst ink based on DLS results.

Sample	D50 (nm)	Size of peak (nm)
D520-40/1	472	480.2
D520-20/1	295	296.9
D520-10/1	310	312.8
D520-5/1	320	322.8

Table S3. ECSA of the catalysts based on Fig. S14 (The specific capacitance considered at 40 μF cm^{-2}).

Sample	Slope (mF cm^{-2})	ECSA (cm^2)
SSC-D72	1.18	29.5
SSC-D79	1.51	37.75
LSC-D520	1.53	38.25
LSC-D521	0.94	23.5

Table S4. Comparison of CO_2RR to C_{2+} performance in various devices.

Catalyst	Current Density (mA cm^{-2})	FE-C_{2+} (%)	J_{C2+} (mA cm^{-2})	Electrolyser	Reference
CuFONC	~25	80.5	~20	H-cell	*Adv. Energy Mater, 2024* [2]
$La_{1.8}Ag_{0.2}CuO_{3.8}$	26	86.4	22.7	H-cell	*Appl. Catal. B-Environ, 2024* [3]
Cu-N-3	43.5	81.9	35.6	H-cell	*J. Am. Chem. Soc, 2023* [4]
ON-CuO	34.6	77	26.6	H-cell	*ACS Catal, 2023* [5]
Cu_2-CuN_3	28	73	20.6	H-cell	*Nat. Com, 2022* [6]
Cu–$CuAlO_2$–Al_2O_3	61.1	85	51.9	H-cell	*J. Am. Chem. Soc, 2022* [7]
$Cu_{500}Ag_{1000}$	400	40	160	Flow cell	*Joule, 2020* [8]
N-modified Cu	400	82.3	329	Flow cell	*Nat. Com, 2021* [9]
Fragmented Cu	300	77.8	233	Flow cell	*J. Am. Chem. Soc, 2022* [10]
Cu-HoMSs	667	77	513.7	Flow cell	*Angew. Chem. Int. Ed, 2022* [11]
BiCu-SAA	400	73.4	294	Flow cell	*Angew. Chem. Int. Ed, 2023* [12]
Al–Cu/Cu_2O	638	84.5	539	Flow cell	*J. Am. Chem. Soc, 2023* [13]
Gd_1/CuO_x	545	81.4	444	Flow cell	*J. Am. Chem. Soc, 2023* [14]
Cu(OH)BTA	500	73	365	Flow cell	*Nat. Com, 2023* [15]
$Cu_{0.5}Zn_{0.5}O_x$	250	76	190	Flow cell	*J. Am. Chem. Soc, 2023* [16]
Cu_2O-NS	~190	81.32	154	Flow cell	*J. Am. Chem. Soc, 2023* [17]
NS-Cu_2O	351	81.7	286	Flow cell	*Adv. Mater, 2024* [18]
Cu-NPs	***600***	***89.4***	***536***	***MEA***	***This Work***

Table S5. Comparison of CO_2RR to C_{2+} performance in MEA setup.

Catalyst	Current Density (mA cm^{-2})	Cell Voltage (V)	FE-C_{2+} (%)	Partial Current-C_{2+} (A)	Reference
Cu-NPs	***600***	***3.57***	***89.4***	***2.15***	***This Work***
Cu-250nm	200	3.9	80	0.8	*Joule, 2019* [19]
Modified Cu	120	3.65	~80	0.48	*Nature, 2020* [20]
Cu/FeTPP	120	3.7	~76	0.46	*Nat. Catal, 2020* [21]
SSC@Cu-PTFE	200	3.9	~75	0.75	*Science, 2021* [22]
Cu_{-DS}	~200	3.5	~70	0.70	*Joule, 2021* [23]
N2SN-Ag-Cu	327	4.5	80	1.05	*Nat. Com, 2021* [24]
Cu-PTFE	175	3.8	80	0.7	*ACS Energy Lett, 2021* [25]
Sputtered Cu	700	3.68	~70	0.78	*Nat. Energy, 2022* [26]
$Cu_2P_2O_7$	350	3.36	73.6	1.03	*Angew. Chem. Int. Ed, 2022* [27]
C/HKUST-1/Cu/PTFE	250	3.8	~75	0.94	*Adv. Mater, 2022* [28]
Cu NPs	400	3.65	70.2	1.4	*Nat. Energy, 2023* [29]
Cu(OH)BTA	241	3.8	73	0.70	*Nat. Com, 2023* [15]
Cu(100)	300	3.8	83	0.25	*Nat. Com, 2024* [30]

Reference:

1. A. Reyes, R. P. Jansonius, B. A. W. Mowbray, Y. Cao, D. G. Wheeler, J. Chau, D. J. Dvorak and C. P. Berlinguette, *ACS Energy Lett.*, 2020, **5**, 1612-1618.
2. Z. Lv, C. Wang, Y. Liu, R. Liu, F. Zhang, X. Feng, W. Yang and B. Wang, *Adv. Energy Mater.*, 2024, DOI: 10.1002/aenm.202400057.
3. G. Dong, G. Wang, J. Cheng, M. Li, Z. Liang, D. Geng and W. Tang, *Appl. Catal., B*, 2024, **342**.
4. W. Xia, Y. Xie, S. Jia, S. Han, R. Qi, T. Chen, X. Xing, T. Yao, D. Zhou, X. Dong, J. Zhai, J. Li, J. He, D. Jiang, Y. Yamauchi, M. He, H. Wu and B. Han, *Journal of the American Chemical Society*, 2023, **145**, 17253-17264.
5. D. G. Park, J. W. Choi, H. Chun, H. S. Jang, H. Lee, W. H. Choi, B. C. Moon, K.-H. Kim, M. G. Kim, K. M. Choi, B. Han and J. K. Kang, *ACS Catal.*, 2023, **13**, 9222-9233.
6. X. Su, Z. Jiang, J. Zhou, H. Liu, D. Zhou, H. Shang, X. Ni, Z. Peng, F. Yang, W. Chen, Z. Qi, D. Wang and Y. Wang, *Nat. Commun.*, 2022, **13**.
7. X. Wang, Y. Jiang, K. Mao, W. Gong, D. Duan, J. Ma, Y. Zhong, J. Li, H. Liu, R. Long and Y. Xiong, *Journal of the American Chemical Society*, 2022, **144**, 22759-22766.
8. C. Chen, Y. Li, S. Yu, S. Louisia, J. Jin, M. Li, M. B. Ross and P. Yang, *Joule*, 2020, **4**, 1688-1699.
9. J.-Y. Kim, D. Hong, J.-C. Lee, H. G. Kim, S. Lee, S. Shin, B. Kim, H. Lee, M. Kim, J. Oh, G.-D. Lee, D.-H. Nam and Y.-C. Joo, *Nat. Commun.*, 2021, **12**, 3765.
10. K. Yao, J. Li, H. Wang, R. Lu, X. Yang, M. Luo, N. Wang, Z. Wang, C. Liu, T. Jing, S. Chen, E. Cortés, S. A. Maier, S. Zhang, T. Li, Y. Yu, Y. Liu, X. Kang and H. Liang, *Journal of the American Chemical Society*, 2022, **144**, 14005-14011.
11. C. Liu, M. Zhang, J. Li, W. Xue, T. Zheng, C. Xia and J. Zeng, *Angew. Chem. Int. Ed.*, 2021, **61**.
12. Y. Cao, S. Chen, S. Bo, W. Fan, J. Li, C. Jia, Z. Zhou, Q. Liu, L. Zheng and F. Zhang, *Angew. Chem. Int. Ed.*, 2023, **62**.
13. L. Zhang, J. Feng, L. Wu, X. Ma, X. Song, S. Jia, X. Tan, X. Jin, Q. Zhu, X. Kang, J. Ma, Q. Qian, L. Zheng, X. Sun and B. Han, *Journal of the American Chemical Society*, 2023, **145**, 21945-21954.
14. J. Feng, L. Wu, S. Liu, L. Xu, X. Song, L. Zhang, Q. Zhu, X. Kang, X. Sun and B. Han, *Journal of the American Chemical Society*, 2023, **145**, 9857-9866.
15. Y. Liang, J. Zhao, Y. Yang, S.-F. Hung, J. Li, S. Zhang, Y. Zhao, A. Zhang, C. Wang, D. Appadoo, L. Zhang, Z. Geng, F. Li and J. Zeng, *Nat. Commun.*, 2023, **14**, 474.
16. C.-J. Chang, Y.-A. Lai, Y.-C. Chu, C.-K. Peng, H.-Y. Tan, C.-W. Pao, Y.-G. Lin, S.-F. Hung, H.-C. Chen and H. M. Chen, *Journal of the American Chemical Society*, 2023, **145**, 6953-6965.
17. P. Wang, S. Meng, B. Zhang, M. He, P. Li, C. Yang, G. Li and Z. Li, *Journal of the American Chemical Society*, 2023, **145**, 26133-26143.
18. C. Li, T. Zhang, H. Liu, Z. Guo, Z. Liu, H. Shi, J. Cui, H. Li, H. Li and C. Li, *Adv. Mater.*, 2024, DOI: 10.1002/adma.202312204.
19. C. M. Gabardo, C. P. O'Brien, J. P. Edwards, C. McCallum, Y. Xu, C.-T. Dinh, J. Li, E. H. Sargent and D. Sinton, *Joule*, 2019, **3**, 2777-2791.
20. F. Li, A. Thevenon, A. Rosas-Hernandez, Z. Wang, Y. Li, C. M. Gabardo, A. Ozden, C. T. Dinh, J. Li, Y. Wang, J. P. Edwards, Y. Xu, C. McCallum, L. Tao, Z. Q. Liang, M. Luo, X. Wang, H. Li, C. P. O'Brien, C. S. Tan, D. H. Nam, R. Quintero-Bermudez, T. T. Zhuang, Y. C. Li, Z. Han, R. D. Britt, D. Sinton, T. Agapie, J. C. Peters and E. H. Sargent, *Nature*, 2020, **577**, 509-513.

21. F. Li, Y. C. Li, Z. Wang, J. Li, D.-H. Nam, Y. Lum, M. Luo, X. Wang, A. Ozden, S.-F. Hung, B. Chen, Y. Wang, J. Wicks, Y. Xu, Y. Li, C. M. Gabardo, C.-T. Dinh, Y. Wang, T.-T. Zhuang, D. Sinton and E. H. Sargent, *Nat. Catal.*, 2019, **3**, 75-82.
22. F. P. G. d. Arquer, *Science*, 2020, **367**, 661-666.
23. Z. Gu, H. Shen, Z. Chen, Y. Yang, C. Yang, Y. Ji, Y. Wang, C. Zhu, J. Liu, J. Li, T.-K. Sham, X. Xu and G. Zheng, *Joule*, 2021, **5**, 429-440.
24. H. Wu, J. Li, K. Qi, Y. Zhang, E. Petit, W. Wang, V. Flaud, N. Onofrio, B. Rebiere, L. Huang, C. Salameh, L. Lajaunie, P. Miele and D. Voiry, *Nat. Commun.*, 2021, **12**, 7210.
25. Y. Xu, J. P. Edwards, S. Liu, R. K. Miao, J. E. Huang, C. M. Gabardo, C. P. O'Brien, J. Li, E. H. Sargent and D. Sinton, *ACS Energy Lett.*, 2021, **6**, 809-815.
26. W. Li, Z. Yin, Z. Gao, G. Wang, Z. Li, F. Wei, X. Wei, H. Peng, X. Hu, L. Xiao, J. Lu and L. Zhuang, *Nat. Energy*, 2022, **7**, 835-843.
27. J. Sang, P. Wei, T. Liu, H. Lv, X. Ni, D. Gao, J. Zhang, H. Li, Y. Zang, F. Yang, Z. Liu, G. Wang and X. Bao, *Angew Chem Int Ed Engl*, 2022, **61**, e202114238.
28. C. A. Obasanjo, G. Gao, J. Crane, V. Golovanova, F. P. Garcia de Arquer and C. T. Dinh, *Nat. Commun.*, 2023, **14**, 3176.
29. A. Ozden, J. Li, S. Kandambeth, X.-Y. Li, S. Liu, O. Shekhah, P. Ou, Y. Zou Finfrock, Y.-K. Wang, T. Alkayyali, F. Pelayo García de Arquer, V. S. Kale, P. M. Bhatt, A. H. Ip, M. Eddaoudi, E. H. Sargent and D. Sinton, *Nat. Energy*, 2023, **8**, 179-190.
30. K. Yao, J. Li, A. Ozden, H. Wang, N. Sun, P. Liu, W. Zhong, W. Zhou, J. Zhou, X. Wang, H. Liu, Y. Liu, S. Chen, Y. Hu, Z. Wang, D. Sinton and H. Liang, *Nat. Commun.*, 2024, **15**, 1749.